

Effect of MIL-53 (Al) MOF particles on the chain mobility and crystallization of poly(L-lactic acid)

Peer-reviewed author version

Kathuria, Ajay; Brouwers, Niels; BUNTINX, Mieke; Harding, Trevor & Auras, Rafael (2017) Effect of MIL-53 (Al) MOF particles on the chain mobility and crystallization of poly(L-lactic acid). In: JOURNAL OF APPLIED POLYMER SCIENCE, 134, p. 1-8 (Art N° 45690).

DOI: 10.1002/APP.45690

Handle: <http://hdl.handle.net/1942/24427>

1 **Effect of MIL-53 (Al) MOF particles on the chain mobility and**
2 **crystallization of Poly(L-lactic acid)**

3 *Ajay Kathuria^{1*}, Niels Brouwers^{1,2}, Mieke Buntinx², Trevor Harding³, Rafael Auras⁴*

4 ¹ Industrial Technology and Packaging, California Polytechnic State University, San Luis
5 Obispo, CA 93407, USA

6 ² Packaging Technology Center, IMO-IMOMEC, Hasselt University, 3590 Diepenbeek,
7 Belgium

8 ³ Materials Engineering, California Polytechnic State University, San Luis Obispo, CA
9 93407, USA

10 ⁴ School of Packaging, Michigan State University, East Lansing, MI, USA 48824-1223

11

12 * Corresponding author:

13 P: (805) 756-2944; F: (805) 756-6111; E: akathuri@calpoly.edu

14

15 *Accepted manuscript Journal of Applied Polymer Science*

16 **Abstract**

17 Polymer-filler interactions significantly influence morphology, functionality and various
18 desirable properties of mixed matrix membranes (MMMs). In this study, chain mobility
19 and crystallization of Poly(L-lactic acid) (PLLA) MMM films prepared by solvent casting
20 PLLA with 1, 5, 10 and 20% wt./wt. of MIL-53(Al) metal organic framework (MOF) were
21 evaluated. The fabricated MMMs were characterized using Differential Scanning
22 Calorimetry (DSC), Fourier Transform Infrared Spectroscopy (FTIR), Thermogravimetric
23 Analysis (TGA), and Scanning Electron Microscopy (SEM). DSC studies indicated that
24 the addition of MOF particles in the PLLA matrix reduces the polymeric chain mobility,
25 which affects the crystallization process. The percent crystallinity of neat PLLA was found
26 to decrease from 4% in neat PLLA to completely amorphous structures in PLLA-10% and
27 PLLA-20% MMMs, as observed in the second heating cycle. FTIR data supports these
28 observations. TGA results showed that PLLA-MOF films are thermally less stable than
29 neat PLLA suggesting that MOF particles act as a depolymerization catalyst for PLLA.
30 Partial agglomeration of MOF particles was observed in the samples using SEM studies.
31 This study indicates strong PLLA-MIL-53(Al) MOF interactions. In addition, this study
32 also provides insight into the effect of MOF particles on the segmental mobility and
33 morphology of PLLA-MIL-53 (Al) composite films.

34

35

36 **1. Introduction**

37 Fillers, functional materials, additives or modifiers have been widely used to improve the
38 functionality of polymeric matrices, including strength, stiffness, hardness, durability,
39 permeability and controlled selective exchange of gases for various applications [1-3].
40 Interfacial interactions between the matrix and filler play an influential role in polymer-
41 filler dynamics. Surface area, concentration and particle size of the filler influence the
42 polymeric chain structure, segmental mobility and crystallinity [4-5]. The interfacial region
43 and its surroundings behave differently from the bulk polymeric matrix. Good polymer-
44 filler interactions can create topological restraints, which may hinder the mobility of
45 polymeric chains. On the other hand, poor interfacial interactions lead to interfacial voids
46 or defects [1, 3, 5-8].

47 Poly(lactic acid) (PLA) is a bio-based, bio-degradable and compostable polymer
48 that has consolidated its market presence due to techno-commercial advancement, growing
49 production capacity and economic viability [9-10]. PLA is a clear, rigid thermoplastic with
50 mechanical strength comparable to poly(ethylene terephthalate) (PET) and polystyrene
51 (PS). However, various inherent limitations such as its brittle nature, poor barrier
52 performance and slow crystallization kinetics limit its wide scale commercial use [1].

53 Metal-organic frameworks (MOFs) belongs to a class of microporous, high surface
54 area crystalline materials synthesized by coordinating metal ions with organic struts [11].
55 Their varied synthesis techniques and potential application in areas such as catalysis, gas
56 storage, gas separation, selectivity, chemical sensing, encapsulation and drug delivery have
57 been comprehensively reported by researchers in the last two decades [11-14]. These

58 reticulate symmetrical crystals can be designed with specific structural properties to meet
59 desired objectives among other organic, inorganic and hybrid porous structures [15-17].

60 MIL-53 (Al) is a highly flexible, thermally and structurally stable, hydrolysis
61 resistant commercially available microporous MOF which is formed by coordination of
62 trivalent aluminum with benzene dicarboxylate struts. It is known for its high surface area,
63 high CO₂ adsorption and selectivity [18, 19]. Ferey *et al.* [20] reported that MIL-53 (Al)
64 has high sorption and selectivity for CO₂ gas over other gases such as O₂ and CH₄. In
65 addition, MIL-53 (Al) is known for its distinct breathing attribute due to the reversible pore
66 expansion and contraction behavior under varying sorbent pressure [21].

67 Ease of processibility and cost effectiveness of the polymers along with high
68 selectivity of MOF particles motivates fabrication of polymer-MOF mixed matrix
69 membranes (MMMs). The polymer-MOF interfacial interaction, polymeric chain mobility,
70 crystallization kinetics and percentage crystallinity of a polymer significantly influences
71 its performance and functionality. Traditionally, interfacial studies have attracted attention
72 in order to achieve higher stress transfer for superior mechanical performance.
73 Additionally, poor interfacial adhesion, or the presence of defects, affects various
74 important properties including gas diffusion and permeability. In the case of polymer-MOF
75 composites, five types of interfacial morphologies have been reported depending on the
76 interfacial interactions are: a). two phase defect free, b). poor interactions leading to voids
77 c). dilated d). increased density e). plugged morphology which can significantly impact
78 their transmission, permeability and perm-selectivity [22]. Such selectively permeable
79 polymer-membranes system can be tailored to gas composition in the headspace of a

80 product-package system to optimize the shelf life of various consumer products including
81 respiring product such as fresh produce, cheese etc.

82 Chain mobility is of great significance during the final stages of polymer
83 processing. In addition, segmental chain mobility can influence the physical aging of
84 polymeric materials, which can alter functional properties particularly in glassy polymers
85 including permeability and selectivity [23-24]. Poly (L-lactic acid) (PLLA), a low
86 entanglement density polymer, has demonstrated further decrease in the entanglement
87 density with physical aging due to segmental mobility of the chains [23]. Such
88 microstructural changes can adversely affect various functional properties including
89 mechanical performance, gas transportation and transparency. Previous studies have linked
90 reduced segmental mobility of polymer-nanocomposites with strong interfacial
91 interactions [1, 24-25]. Segmental mobility of PLA chains is of profound interest as it
92 influences crystallinity, as well as its mechanical, barrier and other functional properties
93 [7-8, 26]. The purpose of this study was to evaluate the effect of MIL-53 (Al) MOF particles
94 on the segmental mobility and crystallization of solvent cast PLLA films. The effect of
95 varying MOFs fraction on the PLLA matrix was analyzed by using an array of
96 characterization techniques.

97 **2. Methodology**

98 **2.1 Materials**

99 Poly(L-lactic acid) (PLLA) resin grade 4043 D, (98% L-lactide) pellets were supplied by
100 NatureWorks LLC (Blair, NE, USA). The weight average molecular weight (M_w) was 111
101 kDa, with a number average molecular weight (M_n) of 84 kDa and a polydispersity index

102 (M_w/M_n) of 1.3. MIL-53 (Al) MOF produced by BASF® was acquired from Sigma-Aldrich
103 (St. Louis, MO, USA) under the trade name of Basolite™ A100 MOF ($C_8H_5AlO_5$), with a
104 surface area between 1,100 and 1,500 m^2g^{-1} and particle size distribution of 31.55 μm .
105 Chloroform [anhydrous $\geq 99\%$] was purchased from Sigma-Aldrich, St. Louis, MO, USA.

106 **2.2 Methods**

107 PLLA pellets were dried at 80 °C for 4 h using a Thermo Fisher Scientific VWR Oven
108 (Fisher Scientific, Waltham, MA, USA) with a negative pressure of 2.93 kPa and packed
109 in an air tight glass bottle. Three grams of dried PLLA pellets were gradually poured into
110 75 mL of chloroform at 23 °C while mixing the solution with a magnetic stir plate (Fisher
111 Scientific, Waltham, MA, USA) at 300 RPM for approximately 90 min until all PLLA
112 pellets were dissolved. Basolite™ A100 MOF ($C_8H_5AlO_5$) particles were crushed by
113 applying light, concentric pressure using a Green Marble Mortar & Pestle. PLLA, PLLA-
114 1% MOF, PLLA-5% MOF, PLLA-10% MOF and PLLA-20% MOF were processed by
115 solvent casting. The desired MOF content was weighed using a Mettler Toledo Scale,
116 Model ME54E (Columbus, OH, USA) and poured in the dissolved PLLA-chloroform
117 solution while mixing the solution with the magnetic stir plate rotating at 300 RPM for 10
118 s. Ultrasonication was performed on the PLLA-MOF-chloroform solution using a Q500
119 ultrasonicator purchased from QSonica, LLC (Newtown, CT, USA). An on-off cycle was
120 programmed to ultrasonicate for 3 min, with an on cycle time of 3 s at a frequency of 20
121 kHz and an alternating off cycle of 0 Hz for 2 s. The ultrasonicated solution was poured
122 into teflon coated molds and covered with two layers of holed Al foil to control the
123 chloroform evaporation rate. After completely evaporating the chloroform, the solid
124 samples were placed in the vacuum oven at 23 °C and a negative pressure of 22 mmHg to

125 extract the residual chloroform from the samples. Samples were stored in vacuum bags at
126 room temperature until the beginning of the different tests. The resulting films had an
127 average thickness of $178 \pm 25 \mu\text{m}$ ($7.00 \pm 1.0 \text{ mil}$).

128 **2.3 Differential Scanning Calorimetry (DSC)**

129 DSC analysis of neat PLLA and PLLA-MIL 53 (Al) MMM films was performed using a
130 DSC Q1000 (TA instruments, DE, USA). Samples size between 5 and 10 mg were
131 obtained from the films and non-hermetically sealed in an aluminum pan and placed with
132 the reference pan in the DSC cell and run in triplicates. Heat/cool/heat cycles from $0 \text{ }^\circ\text{C}$ to
133 $180 \text{ }^\circ\text{C}$ at a rate of $10 \text{ }^\circ\text{C min}^{-1}$ were performed under a constant nitrogen flow of 50
134 mL/min. To disregard the thermal history during processing or storage, the second heating
135 cycle was used to determine the glass transition temperature (T_g), cold crystallization onset
136 (T_{co}), melting temperature (T_m) and to calculate the enthalpy of cold crystallization (ΔH_c)
137 and fusion (ΔH_m). The percent crystallinity X_c (%) was estimated using the following
138 equation:

$$139 \quad X_c (\%) = \frac{\Delta H_m - \Delta H_c}{\Delta H_m^c (1 - x)} \times 100$$

140 where ΔH_m is enthalpy of fusion; ΔH_c is the enthalpy of cold crystallization; ΔH_m^c is
141 enthalpy of fusion of pure crystalline PLA ($\Delta H_m^c = 93.1 \text{ J/g}$ [27]) and x represents the mass
142 fraction of the MOF in the films. Universal Analysis software version 2000 (TA
143 Instruments, DE, USA) was used to analyze the data. Samples were run in triplicates.

144 **2.4 Fourier Transform Infrared Spectroscopy (FTIR)**

145 Fourier Transform Infrared Spectroscopy (FTIR) of MIL 53 (Al) MOF, cast PLLA and
146 PLLA-MIL-53 (Al) MMM films was performed using an attenuated total reflectance

147 (ATR) module attached to FTIR model IRAffinity-1S (Shimadzu, CA, USA). The spectra
148 were acquired in absorption mode at room temperature in the range of 4000-400 cm^{-1} at 2
149 cm^{-1} resolution using 40 accumulated scans. The background spectra used for reduction
150 were collected at room temperature and samples were examined in triplicates.

151 ***2.5 Thermogravimetric Analysis (TGA)***

152 Thermogravimetric analyses of MIL-53 Al-MOF, neat PLLA and PLLA-MOF films were
153 investigated using a TGA Q50 (TA instruments, DE, USA) under sample nitrogen flow of
154 60 mL min^{-1} and balance purge flow of 40 mL min^{-1} . Samples between 5 and 10 mg were
155 obtained from the films and were placed in an aluminum pan before being heated at a rate
156 of 10 $^{\circ}\text{C min}^{-1}$ from room temperature to 600 $^{\circ}\text{C}$. Universal Analysis software version 2000
157 (TA Instruments) was used to analyze the data and samples were run in triplicates.

158 ***2.6 Scanning Electron Microscopy (SEM)***

159 Morphological analysis was performed using a Philips Quanta 200 Environmental
160 Scanning Electron Microscope (FEI, Hillsboro, OR, USA) in low vacuum mode (100 Pa)
161 with the use of a tungsten filament. SEM micrographs of the MOF powder, surfaces of
162 solvent cast PLLA and PLLA-MIL-53 (Al) MMM films were obtained at an accelerating
163 voltage of 12.5 kV.

164 ***2.6 Oxygen Gas Permeability Coefficient***

165 The oxygen transmission rates of the PLLA and PLLA-20% MOF were measured as per
166 ASTM D3985-05 using an Oxtran[®] 2/21 (MOCON Inc., Minneapolis, MN, USA) at 23 $^{\circ}\text{C}$
167 and 0% RH using 100% oxygen gas as permeant and 98 % N_2 / 2% H_2 as the carrier gas at
168 a flow rate of 20 sccm of the test gas and 10 sccm flow rate of carrier gas. The data was
169 collected every 30 min. until stable saturated state was achieved. The transmission rate of

170 4-6 mil thick films was measured using aluminum masks with 3.14 cm² area. The average
171 value of the last ten stable points was used to calculate the permeability values. The data
172 were analyzed for at least three samples.

173 **2.7 Data Analysis**

174 Data analysis was carried out using SAS 9.4 Software (SAS Institute Inc., Cary, NC, USA).
175 Analysis of Variance (ANOVA) was evaluated using Tukey's HSD (Honestly Significant
176 Differences) at 95% confidence interval ($\alpha = 0.05$).

177 **3. Results and discussion**

178 **3.1 Differential Scanning Calorimetry**

179 DSC thermograms of PLLA and PLLA-MIL-53(Al) MMMs are represented in Figure 1.
180 The onset of cold crystallization in PLLA and PLLA-1% MOF was observed at 105.1 and
181 108.6 °C, respectively. A shift in the onset of cold crystallization temperature of the PLLA-
182 1% MOF composition can be attributed to the good interactions between the polymeric
183 chains and the MOF crystals and high surface area of MOF hindering the segmental
184 mobility of the polymeric chains [1, 3, 28]. Such topological constraint can affect
185 crystallization kinetics and viscoelastic properties of the materials. Gagliradi *et al.* [28]
186 studied the interfacial interaction of poly(dimethylsiloxane) with 20 and 40% silica
187 nanoparticles and poly(vinyl acetate) with 40% silica nanoparticles. They observed
188 decreased segmental mobility, which was linked to the specific surface area (SSA) of the
189 nanoparticles, altered chain structure and changed behavior near the interfacial region
190 compared to the bulk polymeric region [28]. The extent of chain restriction also
191 sequentially increased with increase in silica nanoparticle SSA and loading in the
192 polymeric matrix. In another study, Fragiadakis *et al.* [29] reported higher relaxation time

193 in the interfacial region for uniformly distributed natural rubber nano-silica particle based
194 composite systems. In this work, the absence of cold crystallization at higher MOF weight
195 fraction can be ascribed to the fact that more polymeric volume fraction was restricted due
196 to the presence of these particles.

197

<Figure 1>

198 Detailed analysis of the DSC thermograms of PLLA and its composites is provided
199 in Table 1. The increase in the T_g with increase in the MOF loading further indicates
200 reduced segmental mobility. We obtained highly amorphous neat solvent cast PLLA
201 samples with 3.2% crystallinity. The crystallinity further decreased from 3.1 to 0.5% with
202 1 and 5% MOF loading in these composites. PLLA-10% MOF and PLLA-20% MOF were
203 completely amorphous. At these higher MOF loadings, the cold crystallization peaks were
204 absent in the second heating cycle due to reduced chain mobility which could be ascribed
205 to strong polymer-filler interactions. The decreased percentage crystallinity with increase
206 in the MOF content can be correlated to the decreased mobility of the polymeric chains
207 [3]. Although, change in the percentage crystallinity appear to be relatively smaller
208 primarily due to amorphous nature of the polymer. The enthalpy of cold crystallization
209 represented in Table 1 provides a better picture of chain mobility. The enthalpy of chain
210 mobility of PLLA decreased from 8.7 J.g^{-1} to 2.7 J.g^{-1} with the addition of the 1% MIL-53
211 (Al) MOF. We did not observed any cold crystallization peaks at higher MOF loadings.

212

< Table 1>

213

214 3.2 Thermogravimetric Analysis (TGA)

215 Figure 2a and 2b show TGA thermograms and derivative profiles for MOF, neat PLLA
216 and PLLA-MOF films. The first significant weight loss peak observed between 130-140
217 °C can be ascribed to the small weight loss (2-3%) of volatile compounds such as
218 chloroform used for solvent casting or water molecules entrapped in the plastic. Data
219 obtained from TGA thermograms is presented in Table 2. Degradation peaks were not
220 observed in MOF below 500°C due to its high thermal stability [30]. The onset of thermal
221 degradation of PLLA, PLLA-1% MOF, PLLA-5% MOF, PLLA-10% MOF and PLLA-
222 20% MOF was observed at 341.6, 330.9, 321.6, 319.6 and 315.2 °C, respectively. The
223 sharp weight loss observed between 300-376 °C can be ascribed to the thermal degradation
224 of the polymeric chains. Degradation peaks as obtained from derivative profile were
225 observed at 376.6, 359.3, 354.1, 351.2 and 354.5 °C for PLLA, PLLA-1% MOF, PLLA-
226 5% MOF, PLLA-10% MOF and PLLA-20% MOF, respectively. It was also observed that
227 PLLA-MOF composites weight loss peaked around 2.5 %.^{°C}⁻¹ whereas PLLA degradation
228 peaked to 2.35 %.^{°C}⁻¹. The decrease in the onset of thermal degradation temperature,
229 decrease in the degradation peak temperature and increase in the weight loss rate as
230 observed in the first derivative profile (Figure 2b) with the addition of MOF samples can
231 be associated with the MOF particles acting as depolymerization catalysts, which reduced
232 the thermal degradation activation energy [31-33]. Transition metal based complex
233 compounds including MOF particles have been widely recognised for their catalytic
234 activity due to their partial filled d-orbitals or unsaturated metal sites [34]. Fan *et al.* [32]
235 studied thermal degradation of PLLA in the presence of either 5 wt% calcium oxide (CaO)
236 or 5 wt% magnesium oxide (MgO). Based on the differential thermogravimetric profiles,

237 they observed that onset of thermal degradation of PLLA dropped from 270 to 180 and
238 210°C for PLLA-5% CaO and PLLA-5% MgO systems, respectively. Dai *et al* [35]
239 fabricated PLA composites with Zn (II) - pyridine 2,5 dicarboxylate MOF. They also
240 observed decreased thermal stability of PLA at elevated temperatures, which was ascribed
241 to unzipping depolymerization. On the other hand, the degradation of PLA has been
242 reported to be a complex phenomenon due to random scissions leading to linear and cyclic
243 oligomers, which can potentially recombine leading to complex byproducts [35, 36].

244

< **Figure 2a and 2b, Table 2**>

245 **3.3 Fourier Transform infrared spectroscopy (FTIR)**

246 To understand the effect of MOF on the PLLA polymeric matrix, PLLA and MOF peaks
247 were superimposed, and peaks which exist only in PLLA matrix were discriminated for
248 further analysis. Figure 3a provides the FTIR spectra of PLLA and PLLA-MIL-53 (Al)
249 MMMs. The FTIR peaks between 2850 and 3000 cm^{-1} have been assigned to the symmetric
250 and asymmetric stretch of methyl and methylene groups. Medium intensity asymmetric -
251 CH_3 vibration (stretching) and symmetric $-\text{CH}_3$ vibration (stretching) have been observed
252 at 2977 and 2952 cm^{-1} . Various factors can significantly impact peak intensity strength of
253 these bands depending on the structure, chain architecture, and packing [37-40]. In
254 addition, orientation, crystallinity and chain restriction can also affect the intensity of
255 various vibrational peaks [41]. We observed a significant decrease in the peak intensity of
256 $-\text{CH}_3$ (asymmetric and symmetric), carbonyl, and C-O-C group vibrations with addition of
257 1 wt. % MOF particles in the PLLA matrix compared to that of the neat PLLA. This
258 decrease can be related to decreased crystallinity and hindered mobility of the PLLA chains
259 due to the strong favorable interfacial interactions between PLLA and MOF particles [1,

260 42-43]. Yu *et al* [42] reported decreased FTIR peak intensity for poly(vinylidene fluoride)
261 in 2850 to 3000 cm^{-1} wavenumber region with the addition of nanoclay. The decreased
262 intensity was ascribed to the strong interaction between polymer and clay platelets which
263 impeded the chain mobility resulting in reduced infrared absorption in this region. The
264 systematically amplified intensity decrease with the increase in the nano-clay content from
265 0.2 to 10 wt% clay also supports the DSC observations.

266 **<Figure 3a>**

267 Figure 3b shows FTIR spectra around 1750 cm^{-1} band generally correlated with
268 $\nu(\text{C}=\text{O})$ interchain dipole-dipole interaction. These interchain dipole-dipole interactions
269 depend on the distance between the chains and are influential when the distance between
270 the C=O neighboring molecules is less than 2.7 Å [43]. Reduced peak intensity indicates
271 reduced interactions which is supported by the decrease in the crystallinity.

272 **<Figure 3b>**

273 FTIR spectra ranging from wavenumbers 100-800 cm^{-1} are presented in Figure 3c.
274 Wavenumber 871 cm^{-1} has been associated to 10_3 helix conformation which has been
275 linked with the alpha crystals in the PLA [37]. The decreased intensity around this
276 wavenumber is also indicative of the reduced crystallinity due to reduced mobility of PLA
277 chains.

278 **<Figure 3c>**

279 **3.4 Scanning Electron Microscopy (SEM)**

280 Figure 4 a-f show SEM images of MOF particles, PLLA and various compositions of
281 PLLA-MIL-53 (Al) MMMs. Poor polymer MOF interactions can result in non-selective

282 interfacial voids. Therefore, a defect free morphology with strong interfacial interaction
283 between filler and polymeric matrix is a precondition to obtaining superior functional
284 performance of these membranes. We observed defect free polymer-filler morphology for
285 PLLA-MIL-53 (Al) MMMs in Figure 4 c to f, which supports our finding of strong
286 interactions between PLLA and MIL-53 (Al) MOF as also supported by DSC and FTIR
287 studies.

288

<Figure 4 a-f>

289 ***3.5 Oxygen Permeability***

290 Various industrial or consumer applications such as fresh produce packaging may desire
291 selective and tailored oxygen gas permeability. Controlled oxygen gas permeability may
292 help in extending the shelf life of respiring produce. For oxygen mass transfer 20 wt%
293 MIL-53 (Al) was carefully chosen based on the previous research works its quadrupole
294 moment and polarizability [3, 19, 44-45]. Table 3 shows O₂ permeability coefficients of
295 PLLA and PLLA-20% MIL-53 (Al) MOF. Oxygen permeability coefficient increased by
296 26% with the addition of 20% Mil-53 (Al) MOF. Improved oxygen gas breathability of
297 these composites can be ascribed to the strong interactions between organic linkers and
298 oxygen gas molecules [19].

299 **4. Conclusions and Future Work**

300 In this study, PLLA, PLLA- 1% MIL-53(AI), PLLA- 5% MIL-53(AI), PLLA- 10% MIL-
301 53(AI) and PLLA- 20% MIL-53(AI) MMM films were fabricated using a solvent casting
302 process. DSC, FTIR and SEM data supported good interfacial interactions between PLLA
303 and MIL-53(AI) MOF. Favorable polymer-filler interactions reduced segmental mobility
304 of the chain affecting the crystallinity. Completely amorphous PLLA-MIL-53(AI) MMM
305 films were obtained at 5 wt.% MOF or above. The presence of MOF increased the rate of
306 degradation of PLLA by de-polymerization reaction as observed in TGA studies. These
307 membranes can easily be fabricated on mass scale by using master-batch and using cast
308 film extrusion provided favorable economics. The future studies can explore the
309 commercialization of these membrane systems.

310 **Acknowledgments**

311 The authors would like to thank funding from Cal Poly State University and Orfalea Mini
312 Summer Support Research Grant. Authors would also like to thank Eric Futak, Jeffrey
313 Norton, Jessie O'Connell, and Nestor Vazquez for help with the experiments. Authors also
314 thank University of Hasselt for allowing Niels Brouwers to study abroad for his graduate
315 research work. Authors are also thankful to IAPRI for awarding Niels Brouwers a
316 scholarship to travel to Cal Poly.

317 **References**

- 318 1. Kathuria A, Abiad MG, and Auras R. Toughening of poly(L-lactic acid) with Cu_3BTC_2 metal
319 organic framework crystals. *Polymer* 2013; 54: 6979-6986.
- 320 2. Kathuria A, Al-Ghamdi S, Abiad MG, and Auras R. The influence of $\text{Cu}_3(\text{BTC})_2$ metal organic
321 framework on the permeability and perm-selectivity of PLLA-MOF mixed matrix membranes.
322 *Journal of Applied Polymer Science* 2015; 42764 (1-10).
- 323 3. Kathuria A, Abiad MG, and Auras R. Deterioration of metal-organic framework crystal
324 structure during fabrication of poly(L-lactic acid) mixed-matrix membranes. *Polymer*
325 *International* 2013; 62: 1144-1151.
- 326 4. Saiter A, Delpouve N, Dargent E, Oberhauser W, Conzatti L, Cicogna F, Passaglia E. Probing
327 the chain segment mobility at the interface of semi-crystalline polylactide/clay
328 nanocomposites. *European Polymer Journal* 2016; 274-289.
- 329 5. Jiang N, Endoh MK, Koga T, Masui T, Kishimoto H, Nagao M, Satija SK, Taniguchi T.
330 Nanostructures and Dynamics of Macromolecules Bound to Attractive Filler Surfaces. *ACS*
331 *Macro Letters* 2015; 4: 838-842.
- 332 6. Robertson CG, Lin CJ, Rackaitis M, and Roland CM. Influence of particle size and polymer-
333 filler coupling on viscoelastic glass transition of particle-reinforced polymers. *Macromolecules*
334 2008; 41: 2727-2731.
- 335 7. Cho SY, Park HH, Yun YS, and Jin H-J. Influence of Cellulose nanofibers on the morphology
336 and physical properties of poly(lactic acid) foaming by supercritical carbon dioxide.
337 *Macromolecular Research* 2013; 21: 529-533.
- 338 8. Mofokeng JP, Luyt AS, Tabi T, and Kovacs J. Comparison of injection moulded natural fibre-
339 reinforced composites with PP and PLA as matrices. *Journal of Thermoplastic Composite*
340 *Material* 2011, 25: 927-948.
- 341 9. Castro-Aguirre E, Iniguez-Franco F, Samsudin H, Fang X, and Auras R. Poly(lactic acid)-Mass
342 production, processing, industrial applications, and end of life. *Advanced Drug Delivery*
343 *Reviews* 2016; 107: 333-366.
- 344 10. Saeiddlou S, Huneault MA, Li H, and Park CB. Poly(lactic acid) crystallization. *Progress in*
345 *Polymer Science* 2012; 37: 1657-1677. *Nature* 1999; 402: 276-279.
- 346 11. Li H, Eddaoudi M, O'Keeffe M, and Yaghi OM. Design and synthesis of an exceptionally
347 stable and highly porous metal-organic framework.
- 348 12. Rastogi S, Yao Y, Lippits DR, Höhne GWH, Graf R, Spiess HW, Lemstra PJ. Segmental
349 mobility in the non-crystalline regions of semicrystalline polymers and its implications on
350 melting. *Macromolecular Rapid Communication* 2009; 30: 826-839.
- 351 13. Al-Ghamdi S, Kathuria A, Abiad M and Auras R. Synthesis of nanoporous carbohydrate metal-
352 organic framework and encapsulation of acetaldehyde. *Journal of Crystal Growth* 2016; 451:
353 72-78.
- 354 14. Lee JY, Farha OK, Roberts J, Scheidt KA, Nguyen ST, and Hupp JT. Metal-organic framework
355 materials as Catalyst. *Chemical Society Reviews* 2009; 38: 1450-1459.
- 356 15. Kreno LE, Leong K, Farha OK, Allendorf M, Duyne RPV, and Hupp JT. Metal-Organic
357 Framework Materials as Chemical Sensors. *Chemical Reviews* 2012;

- 358 16. Porous metal-organic framework nanoscale carriers as a potential platform for drug delivery
359 and imaging. *Nature Materials* 2010; 9: 172-178.
- 360 17. James SL. Metal-organic frameworks. *Chemical Society Reviews* 2003; 32: 276-288.
- 361 18. Mihaylov M, Chakarova K, Andonova S, Drenchev N, Ivanova E, Pidko EA, Sabetghadam A,
362 Seoane B, Gascon J, Kapteijn F, and Hadjiivanov K. Adsorption of CO₂ on MIL-53 (Al): FTIR
363 evidence of the formation of dimeric CO₂ species. *Chemical Communications* 2016; 52: 1494-
364 1497.
- 365 19. Rallapalli P, Prasanth KP, Patil D, Somani RS, Jasra RV, Bajaj HC. Sorption studies of CO₂,
366 CH₄, N₂, CO, O₂ and Ar on nanoporous aluminum terephthalate [MIL-53(Al)]. *Journal of*
367 *Porous Materials* 2011; 18: 205-210.
- 368 20. Férey G, Latroche M, Serre C, Millange F, Loiseau T and Percheron-Guégan A. Hydrogen
369 adsorption in the nano-porous metal benzenedicarboxylate M(OH)(O₂C-C₆H₄-CO₂) (M =
370 Al³⁺, Cr³⁺), MIL-53. *Chemical Communications* 2003; 2976-2977.
- 371 21. Bourrelly S, Llewellyn PL, Serre C, Millange F, Loiseau T, and Férey G. Different Adsorption
372 Behaviors of Methane and Carbon Dioxide in the Isotypic Nanoporous Metal Terephthalates
373 MIL-53 and MIL-47
- 374 22. Vinh-Thang H, and Kaliaguine S. Predictive models for mixed-matrix membrane performance:
375 A review; *Chemical Review* 2013; 113:4980-5028.
- 376 23. Pan P Zhu B and Inoue Y. Ethalpy relaxation and embrittlement of poly(L-lactide) during
377 physical aging. *Macromolecules* 2007; 40: 9664-9671.
- 378 24. Cangialosi D, Boucher VM, Alegria A, and Colmenero J. Physical aging in polymers and
379 polymer nanocomposites: recent results and open questions. *Soft Matter* 2013; 9: 8619-8630.
- 380 25. Napolitano S, and Wubbenhorst M. The life time of the deviations from bulk behavior in
381 polymers confined at the nanoscale. *Nature Communications* 2011; 2: 260.
- 382 26. Huang HD, Ren PG, Xu JZ, Xu L, Zhong GJ, Hsiao BS, and Li ZM. Improved barrier
383 properties of poly(lactic acid) with randomly dispersed graphene oxide nanosheets. *Journal of*
384 *Membrane Science* 2014; 464: 110-118.
- 385 27. Dorgan J R, *Rheology of Poly(lactic acid)*. *Poly(Lactic Acid): Synthesis, Structures, Properties,*
386 *Processing, and Applications*, Edited by Auras R, Lim L, Selke S and Tsuji H, Wiley Series
387 Published 2010; Chapter 10: 125-139.
- 388 28. Gagliradi S, Arrighia V, Ferguson R and Telling MTF. Restricted dynamics in polymer-filler
389 systems. *Physica B* 2001; 301: 110-114.
- 390 29. Fragiadakis D, Bokobza L, and Pissis P. Dynamics near the filler surface in natural rubber-
391 silica nanocomposites. *Polymer* 2011; 52: 3175-3182.
- 392 30. Loiseau T, Serre C, Huguenard C, Fink G, Taulelle F, Henry M, and bat A rationale for the
393 large breathing of the porous Aluminum Terephthalate (MIL-53) upon hydration.
- 394 31. Motoyama T, Tsukegi T, Shirai Y, Nishida H, and Endo T. Effects of MgO catalyst on
395 depolymerization of poly-L-lactic acid to L,L-lactide. *Polymer degradation and stability* 2007;
396 92: 1350-1358.
- 397 32. Fan Y, Nishida H, Mori T, Shirai Y, and Endo T. Thermal degradation of poly(L-lactide): effect
398 of alkali earth metal oxides for selective L, L-lactide formation. *Polymer* 2004; 45: 1197-1205.

- 399 33. Tsuji H and Fukui I. Enhanced thermal stability of poly(lactide)s in the melt by enantiomeric
400 polymer blending. *Polymer* 2003; 10: 2891-2896.
- 401 34. Yoon JW, Seo Y-K, Hwang YK, Chang J-S, Leclerc H, Wuttke S, Bazin P, Vimont A, Daturi
402 M, Bloch E, Llewellyn PL, Serre C, Horcajada P, Greneche J-M, Rodrigues AE, Ferey G.
403 Controlled Reducibility of a Metal-Organic Framework with Coordinatively unsaturated sites
404 for preferential gas sorption. *Angewandte Chemie* 2010; 122: 6085-6088.
- 405 35. Dai X, Cao Y, Shi X, and Wang X. Non-isothermal crystallization kinetics, thermal degradation
406 behavior and mechanical properties of poly(lactic acid)/MOF composites prepared by melt-
407 blending methods. *RSC Advances* 2016; 2046-2069.
- 408 36. Yu H, Huang N, Wang C and Tang Z. Modeling of poly(L-lactide) thermal degradation:
409 theoretical prediction of molecular weight and polydispersity index. *Journal of Applied*
410 *Polymer Science* 2003; 88: 2557-2562.
- 411 37. *Poly(Lactic Acid): Synthesis, Structures, Properties, Processing, and Applications*, Edited by
412 Auras R, Lim L, Selke S and Tsuji H, Wiley Series Published 2010; Chapter 8: 97-112.
- 413 38. Robinson JW, Frame EMS, Frame II GM. *Undergraduate Instrumental Analysis*, Sixth Edition,
414 MARCEL DEKKER, NY.
- 415 39. Verma SP, Wallach DFH. Raman spectra of some saturated, unsaturated and deuterated C₁₈
416 fatty acids in the HCH-deformation and CH-stretching regions.
- 417 40. Messmer MC, Conboy JC, and Richmond GL. Observation of molecular ordering at the liquid-
418 liquid interface by resonant sum frequency generation. *Journal of the American Chemical*
419 *Society* 1995; 17: 8039-8040.
- 420 41. Paragkumar NT, Edith D and Six JL. Surface characteristics of PLA and PLGA films. *Applied*
421 *Surface Science* 253: 5; 2758-2764.
- 422 42. Yu L and Cebe P. Crystal polymorphism in electrospun composite nanofibers of
423 poly(vinylidene fluoride) with nanoclay. *Polymer* 2009; 50: 2133-2141.
- 424 43. Zhang J, Tsuji H, Noda I, and Ozaki Y. Structural changes and crystallization dynamics of
425 Poly(L-lactide) during the cold-crystallization process investigated by infrared and two-
426 dimensional infra-red correlation spectroscopy. *Macromolecules* 2004; 37: 6433-6439.
- 427 44. Adams R, Carson C, Ward J, Tannenbaum R, Koros W. Metal organic framework mixed matrix
428 membranes for gas separations. *Microporous and Mesoporous Materials* 2010; 131: 13-20.
- 429 45. Elangovan D, Nidoni U, Yuzay I E, Selke SEM and Auras R. *Industrial and Engineering*
430 *Chemistry Research* 2011; 50: 11136-42.

431 **List of Tables**

432 **Table 1.** Thermal characteristics of neat PLLA and PLLA-MIL-53 (Al) MMM films
433 derived from the 2nd heating cycle

434 **Table 2.** Thermo-gravimetric analysis of neat PLLA and PLLA-MOF MMM films

435 **Table 3.** O₂ permeability coefficient of PLLA and PLLA-20% MIL-53 (Al) MOF MMM
436 films

437

438 **List of Figures**

439 **Figure 1.** DSC thermograms of PLLA and PLLA-MIL-53 (Al) MMM films derived from
440 the 2nd heating cycle.

441 **Figure 2a.** TGA of PLLA, MIL-53 (Al) and various PLLA-MIL-53 (Al) MMM films.

442 **Figure 2b.** First derivative weight change as a function of temperature.

443 **Figure 3a.** FTIR Spectra of PLLA and PLLA- MIL-53 (Al) MMM films from wavenumber
444 3000-2800 cm⁻¹.

445 **Figure 3b.** FTIR Spectra of PLLA and PLLA-MIL-53 (Al) MMM films from wavenumber
446 1650-1850 cm⁻¹.

447 **Figure 3c.** FTIR Spectra of PLLA and PLLA-MIL-53 (Al) MMM films from wavenumber
448 950-800 cm⁻¹.

449 **Figure 4.** a). SEM image of MIL-53 (Al), scale size 50 μm b). SEM image of PLLA, scale
450 size 20 μm c). SEM image of PLLA-1% MIL-53 (Al), scale size 20 μm. d). SEM image
451 of PLLA-5% MIL-53 (Al), scale size 20 μm. e). SEM image of PLLA-10% MIL-53 (Al),
452 scale size 20 μm. f). SEM image of PLLA-20% MIL-53 (Al), scale size 20 μm.

453

Table 1. Thermal characteristics of neat PLLA and PLLA-MIL-53 (Al) MMM films derived from the 2nd heating cycle.

Sample	T_g (°C)	Cold Crystallization		Melting		
		T_{co} (°C)	ΔH_c (J/g)	T_m (°C)	ΔH_m (J/g)	X_c (%)
PLLA	56.6 ± 0.5^A	105.1 ± 1.2^A	8.7 ± 1.9^A	148.3 ± 0.4^A	11.7 ± 2.2^A	3.2 ± 0.1^A
PLLA-1% MOF	59.0 ± 0.5^B	108.6 ± 4.2^A	2.7 ± 2.6^B	$149.0 \pm 0.2^{A,B}$	4.7 ± 2.8^B	3.1 ± 0.0^A
PLLA-5% MOF	57.9 ± 0.3^C	-	-	149.4 ± 0.4^B	0.5 ± 0.1^C	0.5 ± 0.1^B
PLLA-10% MOF	$57.3 \pm 1.4^{A,B,C}$	-	-	-	-	-
PLLA-20% MOF	60.1 ± 0.6^B	-	-	-	-	-

454

Note: Values in the same column with same capital superscript letters are not statistically significantly different at $\alpha=0.05$. The “-”symbol denotes no results were obtained due to absence of cold crystallization and melting peaks.

455

456

457

458

459 **Table 2.** Thermo-gravimetric analysis of neat PLLA and PLLA-MOF MMM films.

Sample	Onset Thermal degradation	Weight loss peaks		Peak derivative weight loss
	(°C)	Peak 1 (°C)	Peak 2 (°C)	(%/°C)
PLLA	341.6 ± 2.0 ^A	136.6 ± 2.0 ^A	376.6 ± 1.4 ^A	2.35 ± 0.02 ^A
PLLA-1% MOF	330.9 ± 0.8 ^B	136.5 ± 0.9 ^A	359.3 ± 0.8 ^B	2.50 ± 0.03 ^{A,B}
PLLA-5% MOF	321.6 ± 1.3 ^C	135.7 ± 0.8 ^A	354.1 ± 0.6 ^{C,D}	2.55 ± 0.06 ^B
PLLA-10% MOF	319.6 ± 0.9 ^C	134.6 ± 1.4 ^A	351.2 ± 0.9 ^D	2.52 ± 0.04 ^{A,B}
PLLA-20% MOF	315.2 ± 0.9 ^C	133.3 ± 2.0 ^A	354.5 ± 1.5 ^C	2.51 ± 0.01 ^{A,B}

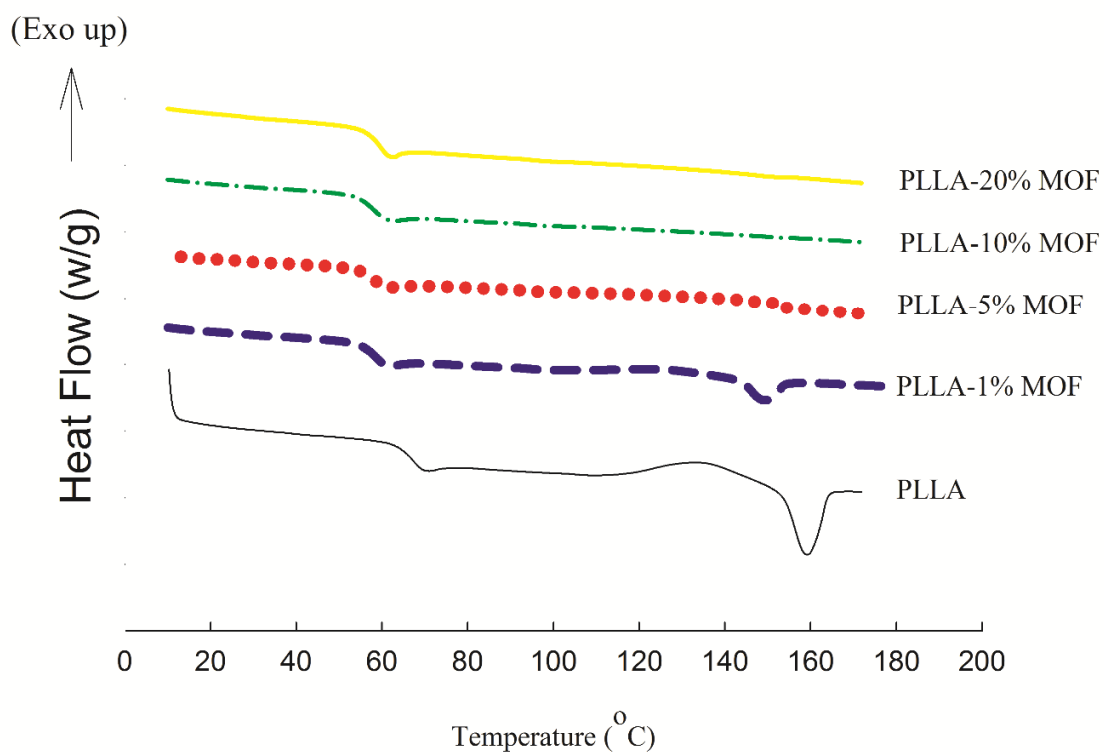
460 *Note:* Values in the same column with same capital superscript letters are not statistically
 461 significantly different at $\alpha=0.05$. The “-” symbol denotes no results were obtained due to absence
 462 of cold crystallization and melting peaks.

463

464 **Table 3.** O₂ permeability coefficient of PLLA and PLLA-20% MIL-53 (Al) MOF MMM
 465 films.

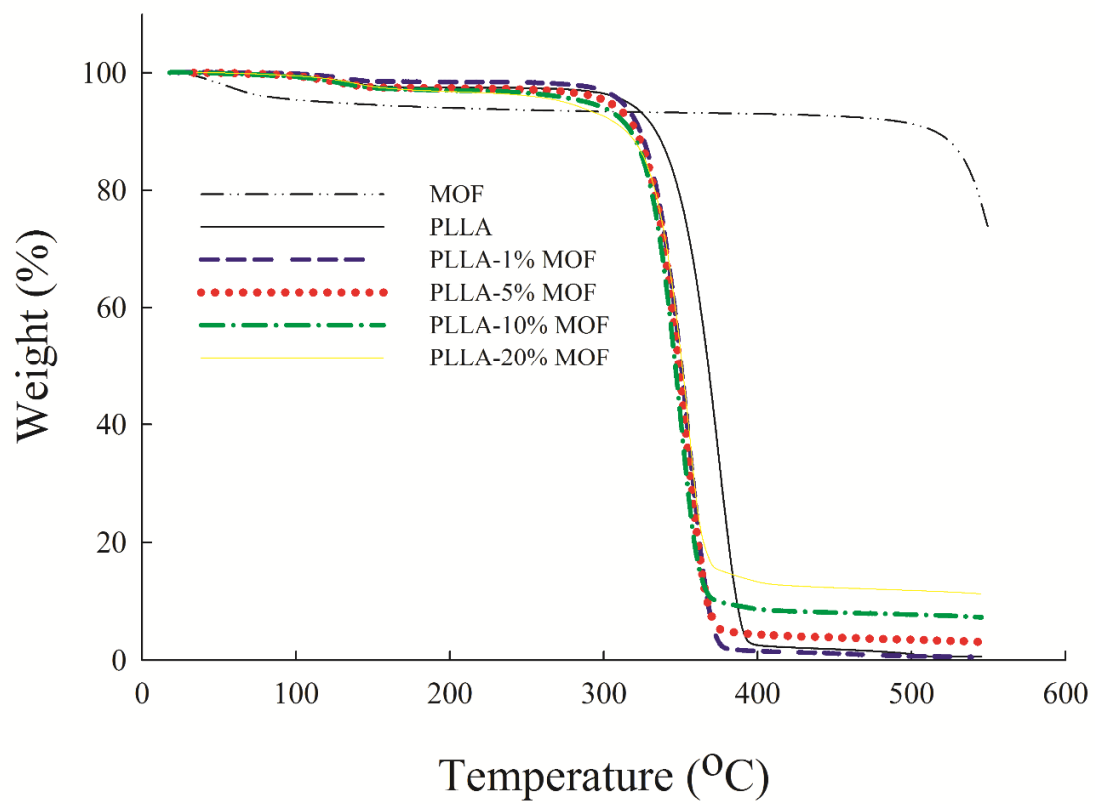
O ₂ Permeability Coefficient x 10 ⁻¹⁸ (kg.m.m ⁻² .s ⁻¹ .Pa ⁻¹)	
PLLA	2.27 ± 0.09 ^A
PLLA-20% MOF	2.87 ± 0.34 ^B

466 *Note:* Values in the same column with same capital superscript letters are not statistically
 467 significantly different at $\alpha = 0.05$.



468

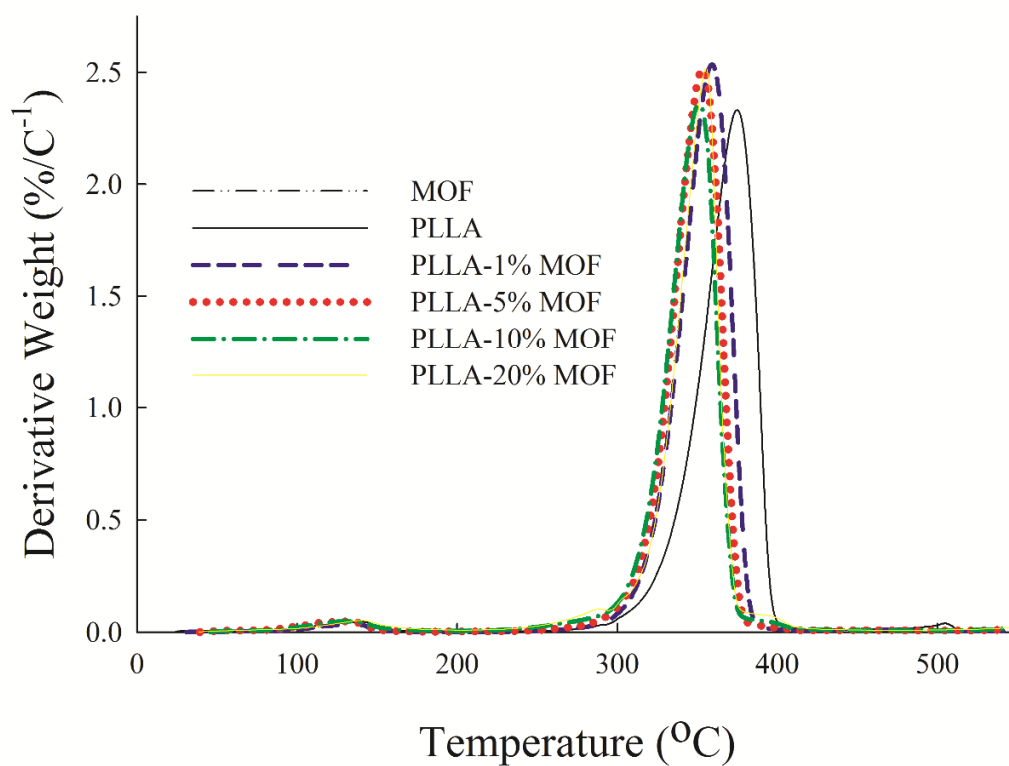
469 **Figure 1.** DSC thermograms of PLLA and PLLA-MIL-53 (Al) MMM films derived from
 470 the 2nd heating cycle.



471

472

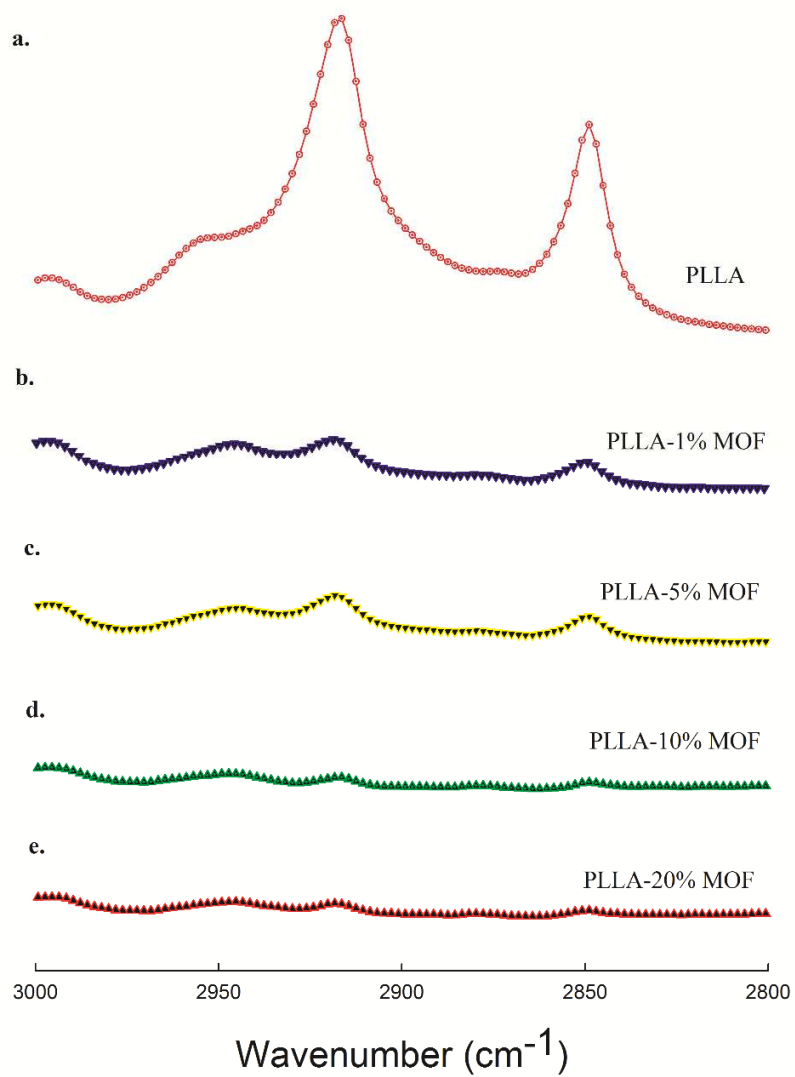
Figure 2a. TGA of PLLA, MIL-53 (Al) and various PLLA-MIL-53 (Al) MMM films.



473

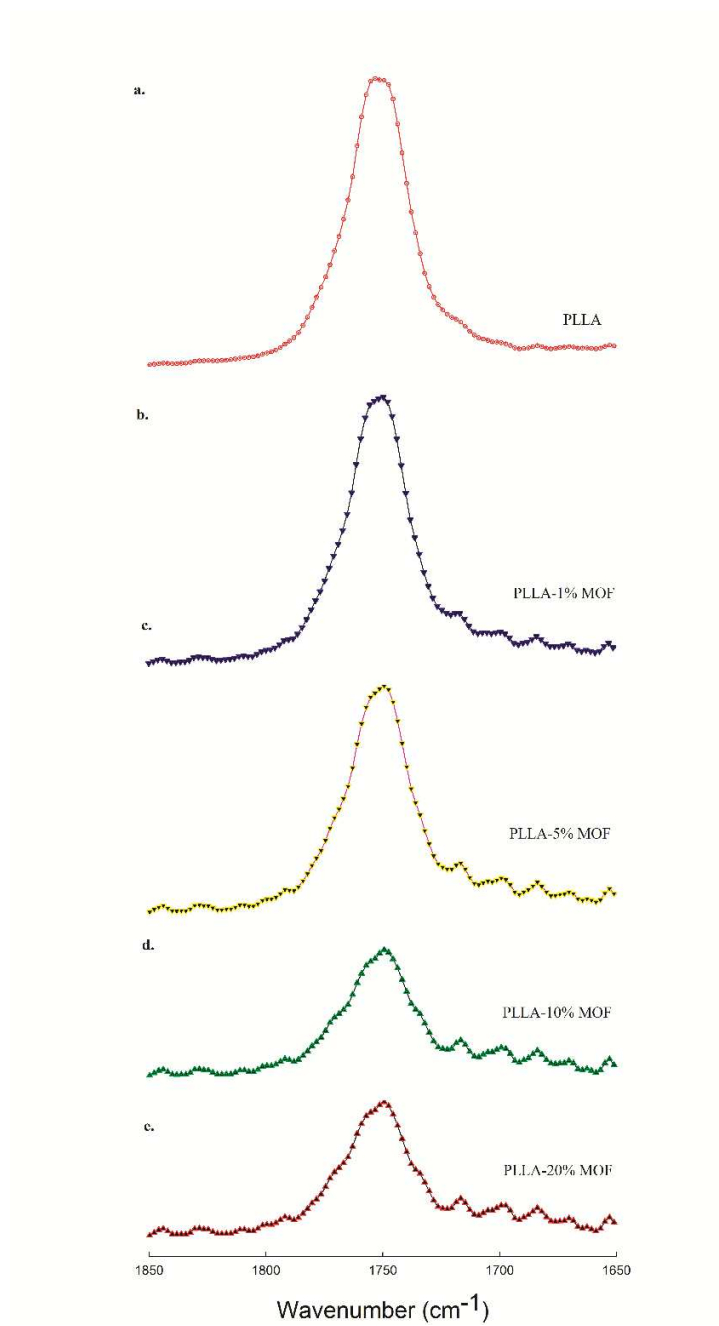
474

Figure 2b. First derivative weight change as a function of temperature.



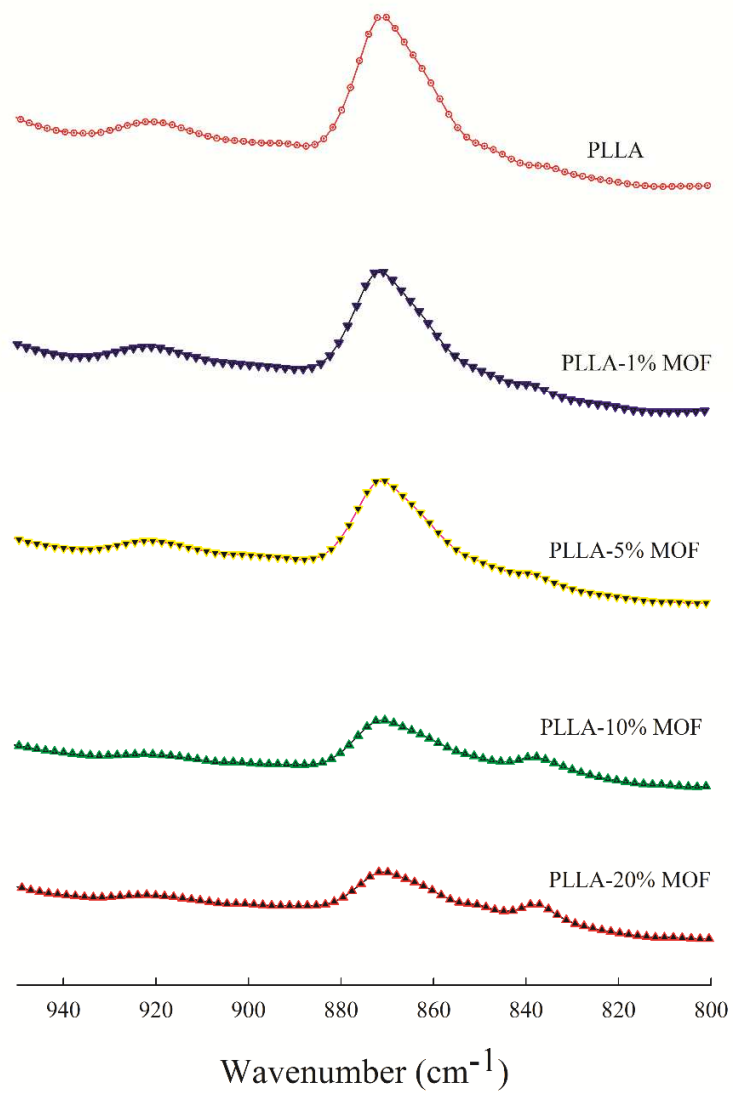
475

476 **Figure 3a.** FTIR Spectra of PLLA and PLLA- MIL-53 (Al) MMM films from wavenumber
 477 3000-2800 cm⁻¹.



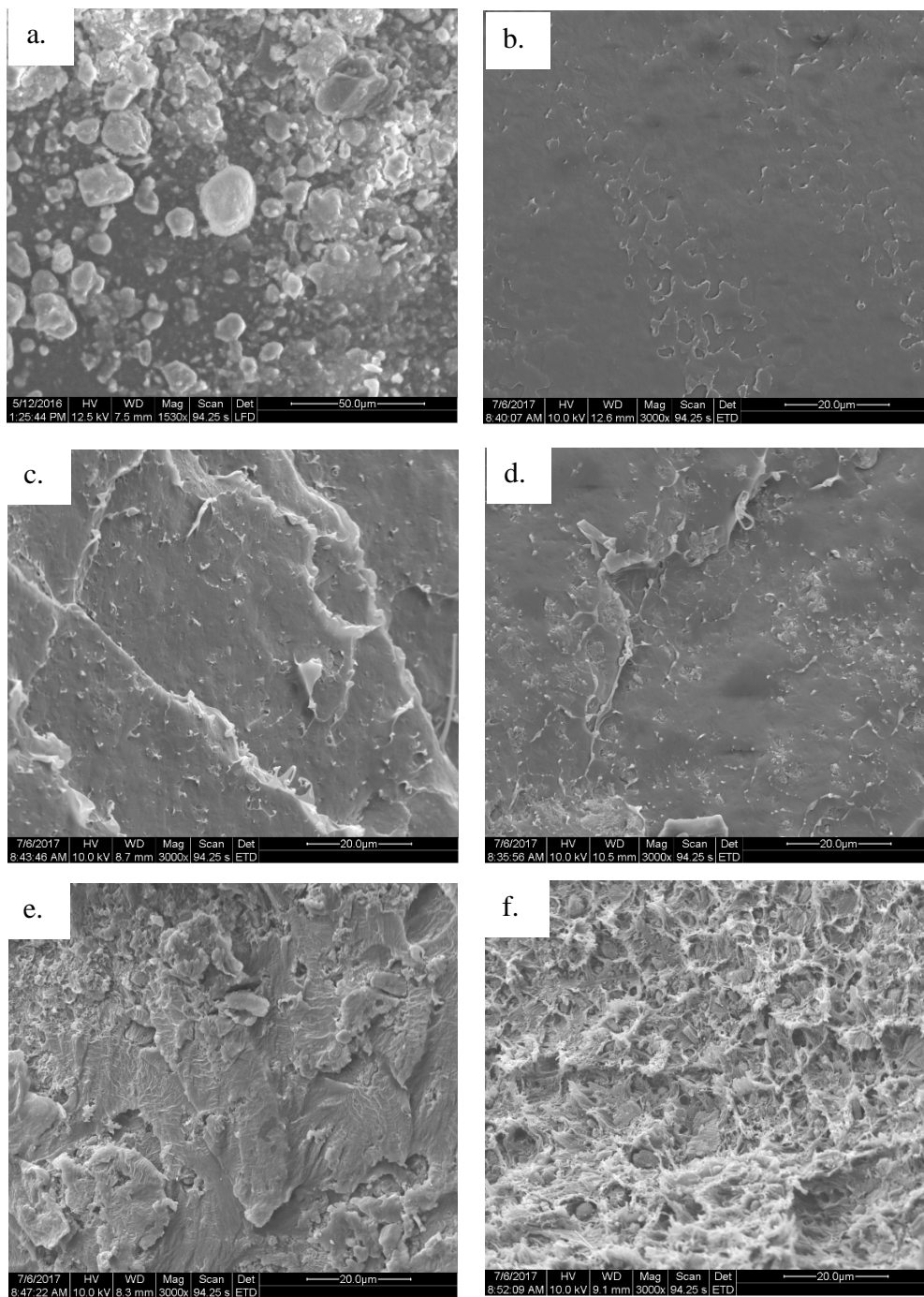
478

479 **Figure 3b.** FTIR Spectra of PLLA and PLLA-MIL-53 (Al) MMM films from wavenumber
480 1650-1850 cm⁻¹.



481

482 **Figure 3c.** FTIR Spectra of PLLA and PLLA-MIL-53 (Al) MMM films from wavenumber
483 950-800 cm^{-1} .



485

486 **Figure 4.** a). SEM image of MIL-53 (Al), scale size 50 μm b). SEM image of PLLA, scale
 487 size 20 μm c). SEM image of PLLA-1% MIL-53 (Al), scale size 20 μm. d). SEM image
 488 of PLLA-5% MIL-53 (Al), scale size 20 μm. e). SEM image of PLLA-10% MIL-53 (Al),
 489 scale size 20 μm. f). SEM image of PLLA-20% MIL-53 (Al), scale size 20 μm.